A&A 662, A80 (2022)
https://doi.org/10.1051/0004-6361/202243192

Astronomy & Astrophysics

Effects of spatial resolution on inferences of atmospheric quantities from simulations

Thore E. Moe[1,2], Tiago M. D. Pereira[1,2], and Mats Carlsson[1,2]

[1] Rosseland Centre for Solar Physics, University of Oslo, PO Box 1029, Blindern 0315, Oslo, Norway
e-mail: t.e.moe@astro.uio.no
[2] Institute of Theoretical Astrophysics, University of Oslo, PO Box 1029, Blindern 0315, Oslo, Norway

Received 25 January 2022 / Accepted 14 April 2022

ABSTRACT

Context. Small-scale processes are thought to be important for the dynamics of the solar atmosphere. While numerical resolution fundamentally limits their inclusion in magnetohydronamic (MHD) simulations, real observations at the same nominal resolution should still contain imprints of subresolution effects. This means that the synthetic observables from a simulation of a given resolution might not be directly comparable to real observables at the same resolution. It is thus of interest to investigate how inferences based on synthetic spectra from simulations with different numerical resolutions compare, and whether these differences persist after the spectra have been spatially degraded to a common resolution

Aims. We aim to compare synthetic spectra obtained from realistic 3D radiative magnetohydrodynamic (rMHD) simulations run at different numerical resolutions from the same initial atmosphere, using very simple methods for inferring line-of-sight velocities and magnetic fields. Additionally we examine how the differing spatial resolution impacts the results retrieved from the STiC inversion code.

Methods. We used the RH 1.5D code to synthesize the photospheric Fe I 617.33 line in local thermodynamic equilibrium (LTE), and the chromospheric Ca II 854.209 line in non-LTE from three MHD simulation snapshots of differing spatial resolution. The simulations were produced by the Bifrost code, using horizontal grid spacing of 6 km, 12 km, and 23 km, respectively. They were started from the exact same atmosphere, and the snapshots were taken after the same exact elapsed time. The spectra obtained from the high-resolution snapshots were spatially degraded to match the lowest resolution. Simple methods, such as the center-of-gravity approach and the weak field approximation, were then used to estimate line-of-sight velocities and magnetic fields for the three cases after degradation. Finally, the spectra were input into the STiC inversion code and the retrieved line-of-sight velocities and magnetic field strengths, as well as the temperatures, from the inversions were compared.

Results. We find that while the simple inferences for all three simulations reveal the same large-scale tendencies, the higher resolutions yield more fine-grained structures and more extreme line-of-sight velocities and magnetic fields in concentrated spots even after spatial smearing. We also see indications that the imprints of subresolution effects on the degraded spectra result in systematic errors in the inversions, and that these errors increase with the amount of subresolution effects included. Fortunately, however, we find that successively including more subresolution yields smaller additional effects; that is to say, there is a clear trend of diminishing importance for progressively finer subresolution effects.

Key words. line: formation – techniques: spectroscopic – Sun: chromosphere – Sun: photosphere

1. Introduction

Small-scale magnetic fields are believed to be strongly linked to the dynamics and heating of the solar atmosphere (see e.g., de Wijn et al. 2009; Martínez González & Bellot Rubio 2009; Bello González et al. 2010; Yadav et al. 2020). Today, 3D radiative magnetohydrodynamic (rMHD) simulations are an increasingly important tool to study the evolution and impact of solar magnetic fields (Stein 2012). These simulations are necessarily limited by computational constraints in how finely they can describe the atmosphere. That is, the numerical grid spacing used presents a limit for how small spatial features can be included. Observations also have finite spatial resolution, but they still contain imprints of subresolution effects. Small-scale motions still happen in the atmosphere even if they are not resolved by our telescopes. This is in contrast to simulations, where a voxel really does represent the smallest details available. It is therefore difficult to directly compare simulations and observations at the same nominal resolution. In most studies (e.g., Khomenko et al. 2005; Pereira et al. 2009; Danilovic et al. 2010; Smitha et al. 2021), synthetic spectra from high-resolution numerical simulations are spatially (and spectrally) degraded using convolutions with point spread functions (PSFs) and downsampled to match observational resolutions. In such studies, the discussion of resolution effects is limited to the mapping between the simulation and the observations. The questions we address here are of a different nature. They are focused on the effects of inferring physical quantities from spectra captured at lower resolutions. In the absence of in situ measurements, spectra remain the primary way to infer physical quantities in stellar atmospheres. The accuracy of such inferrals, whether performed directly from spectra (e.g., Doppler shifts) or via inversions, critically depends on the parameters of the observation, such as spectral and spatial resolution, stray light, and other instrumental effects. The complex problem of stray light can also be seen as a spatial degradation, and many ways to mitigate it have been proposed over several decades (e.g., Skumanich & Lites 1987; Orozco Suárez et al. 2007; Langangen et al. 2007; van Noort 2012). On the other

hand, the issue of subresolution effects has received scant attention.

The key question we want to answer is what the effects of subresolution are on inferred quantities. Spectra carry subtle signatures of subresolution, which presumably could affect inferred quantities such as line-of-sight velocities or magnetic fields. This cannot be tested with observations alone since they already contain an imprint of all scales taking place on the solar surface. However, it can be studied with synthetic spectra from simulations, which can be generated with different amounts of "subresolution structure". Our question is relevant both from a modeling perspective as well as an observational perspective. From the modeling side, it would be most useful to know how much numerical resolution is enough to study events observed at a given resolution. From the observational side, it would be useful to know how much subresolution effects influence quantities inferred from spectra observed at a given resolution; both for inferring quantities through direct analysis of spectra, or via inversions where typically each observed pixel is assumed to be an independent plane-parallel atmosphere with quantities varying smoothly with height (see review by de la Cruz Rodríguez & van Noort 2017).

2. Methods

2.1. Overall approach

Our approach can be summarized as (1) generating synthetic spectra with different amounts of substructure, (2) inferring physical quantities from them, and (3) analyzing the differences. In this section we detail how we achieved the first two points, and we proceed with the analysis of the results in Sect. 3.

Our basic premise was to generate synthetic spectra from 3D rMHD simulations, where all spectra share the same spatial pixel size. Spectra with no subpixel structure were obtained by direct synthesis from a simulation. In this case, a spatial pixel from the simulation has the same resolution as the spatial pixel of the synthetic spectra. Spectra with subpixel structure were obtained by synthesis from a higher resolution simulation, followed by spatial degradation and rebinning to a lower resolution pixel size, so as to mimic what happens with observed light. As detailed below, our reference "zero subpixel structure" simulation has a horizontal spatial resolution of 23 km pix^{-1}. We then worked with simulations that have two times and four times higher resolutions (approximately 6 and 12 km pix^{-1}). Spectra from the higher resolution simulations were then spatially degraded so that they match the spatial resolution of the canonical simulation and, therefore, have different amounts of subresolution effects. The 6 km pix^{-1} run has imprints of resolution effects up to four times the canonical resolution, and the 12 km pix^{-1} run has up to twice the canonical resolution. In the rest of this section, we give details on the simulations used, how the spectral synthesis was performed, and how physical quantities were inferred from the spectral quantities.

2.2. Simulations

We made use of three same-time rMHD simulation snapshots with a magnetic field configuration similar to that of a coronal hole, which are identical in all respects apart from their spatial resolution. The simulations were run using the Bifrost code (Gudiksen et al. 2011). The challenge was to develop simulations whose state and morphology were as close as possible, with the only difference being the spatial resolution. Our approach was as follows. We started by running a simulation with $1024\times1024\times1024$ grid points, with a horizontal resolution of 12 km pix^{-1} and a vertical resolution that varied (nonequidistant). This simulation was allowed to evolve for about 2.2 h of solar time. At this point, two other simulations were branched off and run in parallel. One of the additional simulations was run with exactly half the number of grid points in each direction ($512\times512\times512$ cells with 23 km pix^{-1} in the horizontal direction), and the other was run with twice as many points in the horizontal directions ($2048\times2048\times1024$ cells with 6 km pix^{-1} in the horizontal direction). The spatial extent and all other simulation parameters were the same in all simulations. All simulations were allowed to evolve for a further 120 s of solar time, and those were the snapshots we used for this work. This time was chosen to balance two opposing considerations: first the simulations should have had sufficient time to relax so that the high resolution structures have coalesced at their appropriate resolution level, secondly the duration should not be so long that the simulations diverge from each other in a macroscopic sense. Inspection of the spatial power spectra for the continuum intensity shows that the power at the smallest scales has just about stabilized at the chosen time, while the power at the large scales remains virtually identical. This gives us some confidence that the chosen snapshots reasonably balance our competing requirements.

As noted before, we use the 23 km resolution simulation as a reference for no spatial subresolution, and the other two for varying amounts of subresolution. This means that we have, in effect, only two data points other than the reference. One could argue that this is insufficient and that one could still experiment with a broader range in resolutions. However, there are also good reasons to keep it at three. First, it is numerically unstable to branch off a simulation with a large difference in spatial resolution compared to the parent simulation. Such simulations would need to be relaxed for longer, and the result would be a simulation where the morphology would have evolved differently from the parent simulation, making it much harder to compare features at the pixel level. Second, since we are degrading the higher resolution simulations to a lower resolution, there will be diminishing returns after a certain resolution. The subresolution imprints on spectra would be smaller and smaller because higher resolution details would be destroyed in the spatial degradation process. For these reasons, we chose to use three simulations.

The simulations cover approximately 12 Mm in the horizontal directions, and they extend from $z = -2.5$ Mm below and up to $z = 8$ Mm above the solar surface ($z = 0$ is defined where average $\tau_{500} = 1$). The vertical grid points are more densely distributed around the chromospheric and photospheric heights, tapering off toward the corona above and the convection zone below (6–8 km spacing in the height range -1 to 3 Mm and increasing to 35 km at the top and 15 km at the bottom of the simulation domain in the high resolution run). The simulations were run with periodic boundary conditions along the horizontal dimensions, and open boundary conditions for the vertical dimension. In all runs we assume hydrogen ionization in local thermodynamic equilibrium (LTE). The magnetic field configuration comes from a small-scale dynamo, with an additionally imposed vertical field having a mean signed B_z of 0.25 mT (2.5 G) and a mean unsigned magnetic field of 3.7 mT at $z = 0$.

Lastly, we would like to provide a note on the spatial resolution and numerical pixel size. With observations, the spatial resolution comes from the diffraction limit of the telescope, which gives the smallest detail observable. With numerical simulations, the relation between the pixel size and smallest detail that can be

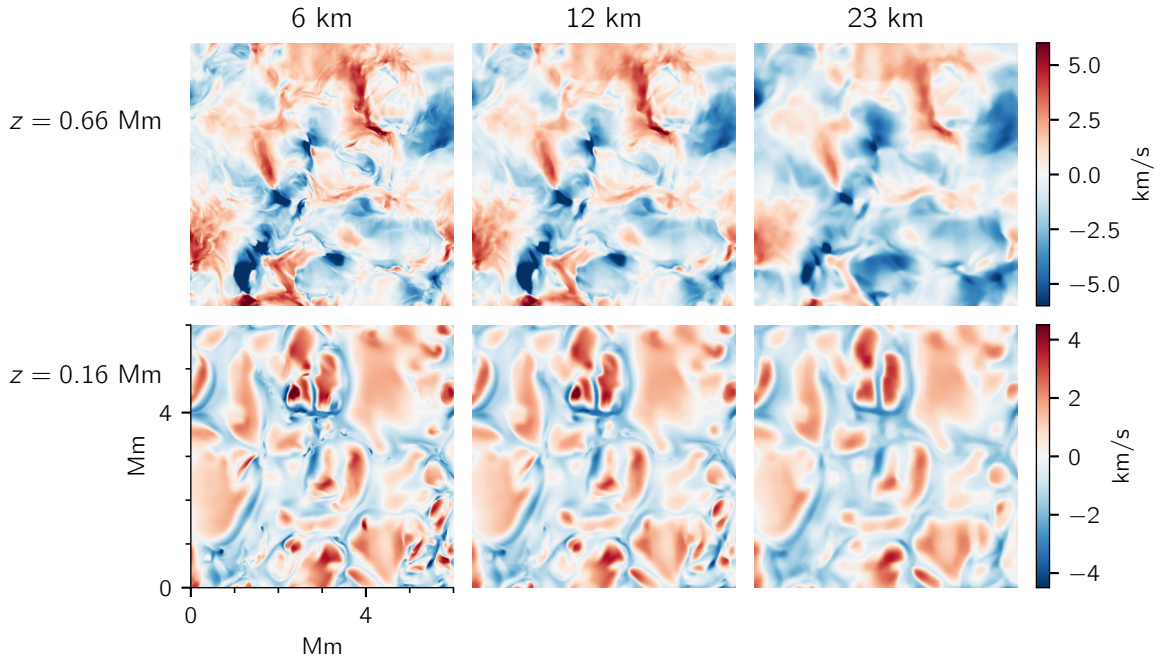

Fig. 1. Line-of-sight velocities taken directly from horizontal slices of the simulations at different heights. The *left column* shows the 6 km simulation, the *middle column* shows the 12 km simulation, and the *right column* shows the 23 km simulation. The *top row* corresponds to a height of 0.66 Mm, i.e., in the low chromosphere, while the *bottom row* corresponds to a height of 0.16 Mm, i.e., in the photosphere. It is important to note that here, and in all subsequent colormaps, we only show a quarter of the full simulation extent in order to more easily see fine details.

reproduced is not so straightforward because of numerical diffusion. Kritsuk et al. (2011) found that numerical dissipation in the STAGGER code (a close relative of Bifrost) leads to considerable damping of scales $\lesssim$5 grid cells. This means that numerical resolution cannot be directly compared to observational resolution since numerical diffusion makes it unlikely for the code to produce small scales down to the grid resolution. For example, in Fig. 1 we show vertical velocities at two heights from the simulations. Looking at sizes of the smallest structures, it is clear they are larger than the pixel sizes. To estimate the real resolution of the 23 km simulation, we performed a simple test. We extracted a high-resolution map of vertical velocities at $z = 0$ from the 6 km simulation (resampled to 23 km pixels) and degraded it to find out how much degradation best agrees with the corresponding map from the 23 km simulation. That is, we consider the high-resolution map as a "ground truth", and we estimated the impact of numerical diffusion as the amount of degradation required until the degraded ground truth matched the map from the 23 km simulation. We found that for a Gaussian convolution, a full width at half maximum (FWHM) of about 5 pixels works best, which is consistent with the results of Kritsuk et al. (2011) for the STAGGER code. This means that the "smallest detail observable," or equivalent observational resolution, of the 23 km simulation is $\approx$5 times the pixel size, or about 115 km.

2.3. Spectral synthesis

To probe the effects of subresolution in the photosphere and in the chromosphere, we synthesized two spectral lines: Fe I 617.33 nm (computed in LTE), and Ca II 854.209 nm (computed in non-LTE, or NLTE). It is important to note that we use air wavelengths throughout this work. The Fe I line is formed in the photosphere and is a commonly used diagnostic for photospheric magnetic fields; in particular it is used by the HMI instrument (Schou et al. 2012). The Ca II 854.209 nm line is formed over a large range of heights, from the photosphere to the chromosphere, and suffers from strong NLTE effects (Leenaarts et al. 2009). There is considerable interest in using this line and its neighboring relatives which together constitute the Ca II infrared triplet for diagnostics of the chromosphere (see e.g., de la Cruz Rodríguez & van Noort 2017; Quintero Noda et al. 2016, 2017).

Both lines were synthesized using the RH 1.5D code (Pereira & Uitenbroek 2015), a publicly available line synthesis code based on the RH code (Uitenbroek 2001). RH 1.5D works on a column-by-column basis, solving the radiative transfer equation treating each column in the 3D simulation as a 1D atmosphere. To save computing time, points above 100 kK in the top of each 1D atmospheric column were not included in the calculation. Line profiles for both lines were computed assuming complete redistribution (CRD). For the NLTE computations of Ca II, we used a model atom with five bound levels plus a continuum level. For both lines, we solved the polarized radiative transfer equation assuming only Zeeman polarization.

The choice of using LTE for the synthesis of Fe I 617.33 nm deserves some further comment. While it has been usual to assume LTE for this line, and the very similar Fe I 630.15/630.25 nm pair, it has long been known that both NLTE effects and 3D effects can have an impact on these photospheric Fe I lines (see e.g., Holzreuter & Solanki 2013; Smitha et al. 2020, 2021 for recent investigations on this subject). In this work, however, we only aim to compare spectra across different spatial resolutions; we are not per se aiming to retrieve the most faithful estimations of the atmospheric parameters possible. Furthermore, the wings of Ca II, which are in fact computed in NLTE, also probe the photosphere and, as we show later, they display the same tendencies for the inferred atmospheric parameters as the LTE Fe I line. We therefore believe the LTE computations of the Fe I-line to be sufficient for our purposes.

The last step was to spatially degrade the spectra from the 6 km and 12 km simulations to a resolution of 23 km, so they could be directly compared with the simulation run at 23 km (the reference simulation with no subpixel structure). For each wavelength in the synthetic profiles, we performed a 2D Gaussian convolution in the spatial domain. The FWHM was 4 pixels for the 6 km simulation and 2 pixels for the 12 km resolution. Lastly, the spectrograms were downsampled to a 23 km pixel size. The end result were spectrograms with the same size as those computed from the 23 km simulation (512×512 columns). No analysis was performed for the 6 and 12 km resolution spectra at their native resolutions. In all subsequent mentions, when we refer to results from 6 km or 12 km, we mean $6 \rightarrow 23$ km or $12 \rightarrow 23$ km: the simulations degraded to a pixel size of 23 km.

2.4. Inferring physical quantities from spectra

Equipped with synthetic spectra with different amounts of subresolution effects, we proceeded to infer physical quantities from them. We start with widely used techniques for deriving line-of-sight velocities and magnetic fields from spectra. Those are detailed below, with different strategies for photospheric and chromospheric values.

2.4.1. Photosphere

To infer the photospheric line-of-sight velocities and magnetic fields, we made use of the Fe I 617.33 nm line. We applied the so-called center-of-gravity (COG) method, following Uitenbroek (2003). The central wavelength of the line was estimated for each pixel as follows:

$$\lambda_{\mathrm{COG}} = \frac{\int \lambda (I_{\mathrm{cont}} - I(\lambda)) \mathrm{d}\lambda}{\int (I_{\mathrm{cont}} - I(\lambda)) \mathrm{d}\lambda}, \tag{1}$$

where λ_{COG} is the estimated central wavelength, I_{cont} is the Stokes I intensity of the nearby continuum, $I(\lambda)$ is the wavelength-dependent Stokes I intensity, and the integral extends over the whole line profile. (It is important to note that SI units are used throughout this work.) In essence, this is a mean wavelength of the profile weighted by the line intensity's departure from the continuum. The position of the central wavelength was then converted to line-of-sight velocity using the Doppler formula, using the convention where positive velocities are upflows.

The line-of-sight magnetic fields can be estimated by

$$B_{\mathrm{LOS}} = \frac{\lambda_+ - \lambda_-}{2} \frac{4\pi m_{\mathrm{e}} c}{e g_{\mathrm{L}} \lambda_0^2}, \tag{2}$$

where B_{LOS} is the line-of-sight magnetic field, m_{e} is the electron mass, e is the electron charge, and g_{L} is the (effective) Landé g factor of the line. We note that g_{L} is 2.5 for Fe I 617.33 nm and 1.1 for Ca II 854.209 nm; an explicit formula for the g factor can be found in Landi Degl'Innocenti & Landolfi (2004). Also, λ_+ and λ_- are the centroids of the circularly polarized line components, right- and left-handed, respectively. These were obtained by replacing $I(\lambda)$ with $I(\lambda) \pm V(\lambda)$ in Eq. (1), where $V(\lambda)$ is Stokes V. We used the convention where positive B_{LOS} are pointing outward.

The same method may be applied to the Ca II line, though in that case it is not the chromospheric line core which is probed, but rather the much wider photospheric line wings, which carry most of the "weight" in the COG method. That is because the full line profile must be integrated over in order to avoid biasing the estimates. From a purely geometric standpoint, the wings of the profile are so much wider than the core that the shape and size of the wings make them contribute much more to the center of gravity. That is why the full-profile application of the COG method is mostly sensitive to the photospheric conditions of the line wings. In order to increase the relative contribution of the core to the COG estimate, one would have to limit the integration window to contain less area in the wings. However, that is challenging to do without introducing a strong bias in the estimates. If, for instance, the integration is not centered on the (Doppler-shifted) line core, more signal would be included from one wing rather than the other, artificially shifting the COG estimate.

2.4.2. Chromosphere

Since the COG method only works well when applied to a full profile, we needed to use a different approach to retrieve information from the chromospheric core of Ca II. Given that we introduced no spectral degradation and the simulations used are of moderately high resolution, the Ca II 854.209 line profiles show great variability near the line core. The core itself is poorly defined, and often many peaks and minima can be found, which complicates the task of extracting a single velocity value. Usual methods such as measuring the shift of the line minimum become unreliable. Given these difficulties and how they affect the simulations considered differently, we believe that inferring chromospheric velocities for our purposes is fraught with uncertainty, and we opted not to estimate chromospheric velocities from spectra.

To estimate the line-of-sight magnetic field strengths in the chromosphere, we were able to employ the weak field approximation (WFA, see Martínez González & Bellot Rubio 2009 and Centeno 2018). We used, corresponding to Eq. (8) in Centeno (2018), the following estimate (in SI units):

$$B_{\mathrm{LOS}} = -\frac{4\pi m_{\mathrm{e}} c}{e g_{\mathrm{L}} \lambda_0^2} \frac{\Sigma_\lambda \frac{\partial I(\lambda)}{\partial \lambda} V(\lambda)}{\Sigma_\lambda (\frac{\partial I(\lambda)}{\partial \lambda})^2}, \tag{3}$$

where the sum is over all wavelength points in the region of interest. For the sake of simplicity, we employed the method on the interval $\lambda_0 \pm 0.05$ nm, which seems to reasonably cover the core for most of our profiles.

2.5. Inferring physical quantities from inversions

Our final means of comparing the effects of spatial resolution is to see how they impact the atmospheres retrieved from inversions. For each of the three cases (6 km degraded to 23 km, 12 km degraded to 23 km, 23 km undegraded), we ran one inversion cycle with both the Fe I and Ca II spectra as input to the state-of-the-art inversion code STiC (de la Cruz Rodríguez et al. 2019). STiC, as RH 1.5D, works on a column-by-column basis. As an initial guess atmosphere for all pixels, we used a 1D model constructed from the 23 km simulation averaged over isosurfaces of column mass. The averaged model was constructed by taking the horizontal average of the atmosphere interpolated at 100 evenly log-spaced points in column mass in the range $[-7, 1]$ kg m^{-2}, and afterward by excluding all but the first point in either direction outside the interval $[-7, 1]$ in $\log(\tau_{500})$ so that regions with no signal from the spectral lines were not included in the inversions. The inversions were performed with 9 nodes for temperature, no microturbulence, and 5 nodes for the line-of-sight magnetic field strength, the horizontal magnetic field

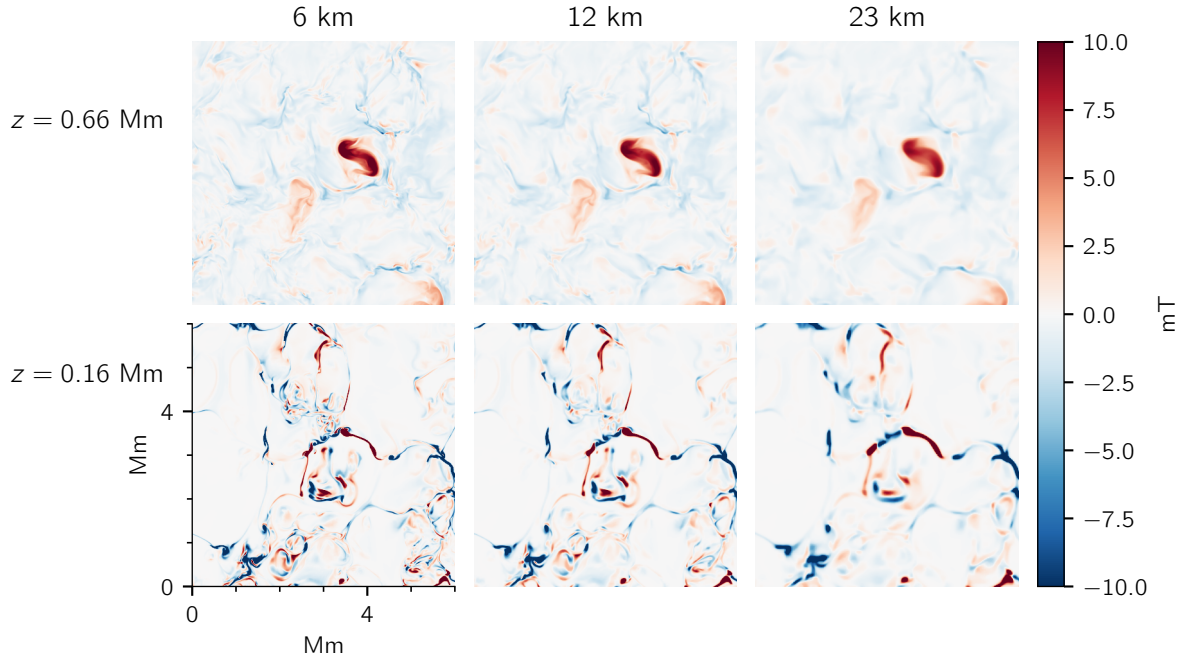

Fig. 2. Line-of-sight magnetic field taken directly from horizontal slices of the simulations at different heights. The *left column* is from the 6 km simulation, the *middle column* is from the 12 km simulation, and the *right column* is from the 23 km simulation. The *top row* shows slices at a height of 0.66 Mm, i.e., in the low chromosphere, while the *bottom row* shows slices at a height of 0.16 Mm, i.e., in the photosphere.

strength, the azimuth angle of the magnetic field, and the line-of-sight velocity.

3. Results

3.1. Comparing the simulations

Figure 1 shows the vertical velocities v_z for the three simulations at chromospheric and photospheric heights at their native resolutions. Only a quarter of the full spatial extent is shown, so as to better show the small details. These two heights were not chosen to correspond with the formation heights of the investigated spectral lines directly. Rather, we want to show the general and qualitative differences between the simulations in the photosphere and chromosphere. We see that, although all three simulations show very much the same large-scale picture, the higher-resolution simulations display fine-structure that is absent in the lower-resolution cases. Furthermore, they contain localized "hotspots" showing more extreme line-of-sight velocities than in the 23 km simulation.

The same story is corroborated through Fig. 2, which shows the simulations' vertical magnetic fields B_z at chromospheric and photospheric heights. The differences in fine-structure are particularly noticeable in the bottom panel, but they can also be seen in the top panel. As for the vertical velocities, localized areas appear where the field strengths are more extreme in the high-resolution cases.

3.2. Photospheric inferences from spectra

Turning our attention to the physical quantities inferred from the spectra, we first look at the information gleamed from the Fe I 617.33 nm line. The three columns of Fig. 3 show the inferred line-of-sight velocities (top) and magnetic fields (bottom) for this line, using the COG method, for the three resolution cases after spatial degradation to the same nominal resolution, that is to say 6 km degraded to 23 km, 12 km degraded to 23 km, and 23 km undegraded, going from left to right.

As seen in the quantities from cuts in the simulations, the inferred line-of-sight velocity and magnetic field strength maps continue to show the same large-scale structures. But interestingly, even after the spatial degradation to the same nominal resolution of 23 km, significant differences in fine-structure and extrema persist between the three cases. In particular, as the underlying resolution of the simulation increases, there is a tendency, in tandem, of more fine-structure and more extreme hotspots.

In Fig. 4 we show the corresponding line-of-sight velocity and magnetic field maps derived from the Ca II 854.209 nm line. As before, these maps were obtained using the COG method over the whole line profile. As mentioned in Sect. 2.4.1, the contribution from the line wings dominates and gives results which are clearly photospheric in nature. Though not exactly matching Fig. 3, the same features and tendencies can be observed in this case as well. In accordance with the photospheric slices of the simulations in Figs. 2 and 1, we see increasing fine-structure and extrema with increasing resolution. While the Fe I line and the Ca II wings are not formed at the same heights, the striking similarities between the line-of-sight velocities and field strengths retrieved from them and the photospheric simulation slices lends confidence to our choice of ignoring NLTE effects in the Fe I synthesis. That is, the effects of spatial resolution appear similar in the photosphere for both LTE and NLTE synthesis, at least for the currently considered case.

In Fig. 5 we show the histograms of both quantities for the two lines taken for the full horizontal extent of the simulations, not just the smaller field of view shown in the previous figures. These corroborate our qualitative discussion above. The left column, showing the logarithmic distribution of the inferred line-of-sight velocities for Fe I (top) and Ca II (bottom), displays the tendency of increased extremes in the line-of-sight velocity with increased resolution. While the jump from 23 km to

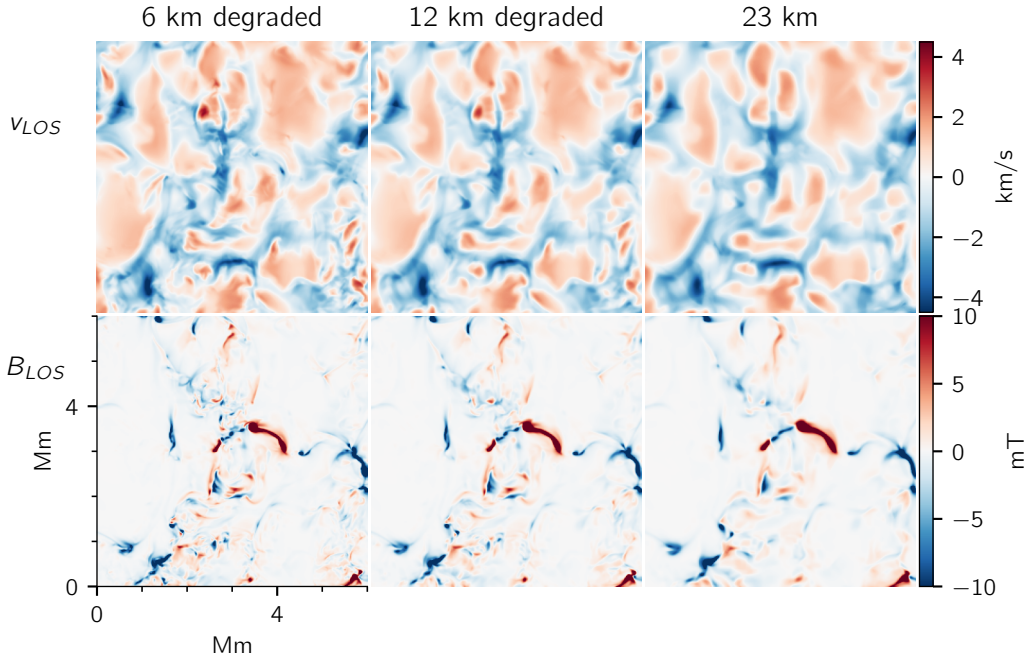

Fig. 3. Inferred line-of-sight velocities and magnetic fields for Fe I 617.33 nm. The *top row* shows the line-of-sight velocities computed by the COG method, while the *bottom row* shows the line-of-sight magnetic fields calculated by the COG method. The *left column* shows the results from the degraded 6 km simulation (degraded to match the resolution of the 23 km simulation), the *middle-right column* shows the results from the degraded 12 km simulation (degraded to match the resolution of the 23 km simulation), and the *right column* shows the results for the (undegraded) 23 km simulation.

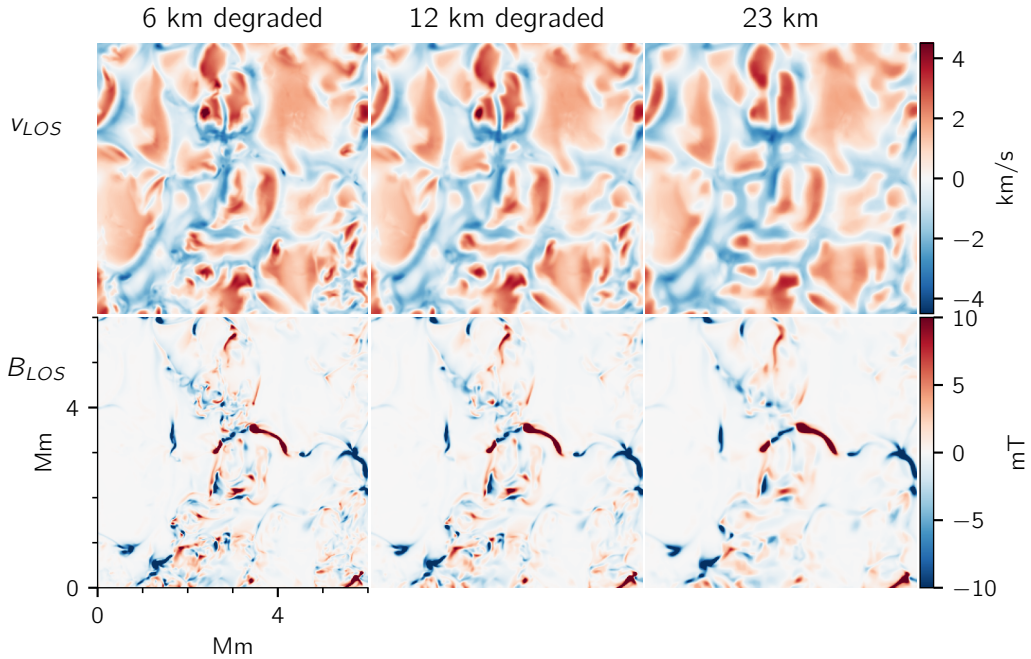

Fig. 4. Inferred line-of-sight velocities and magnetic fields for Ca II 854.209 nm, using the COG method over the whole line profile (core and wings). The layout is exactly the same as in Fig. 3.

12 km notably seems more significant than the one from 12 km to 6 km, the line-of-sight velocities do not appear converged yet. The right column, showing the logarithmic distribution of the inferred line-of-sight magnetic field strengths, shows a more equivocal case. It is clear that the distribution is pushed to larger extremes for the degraded 6 km and 12 km cases compared to inferences from the native 23 km simulation. Here, however, it seems that the extremities do not grow much from the 12 km to 6 km resolution. But, as we saw in Figs. 3 and 4, even with comparable extreme values, the fine-structure has not converged in the 12 km case.

3.3. Chromospheric inferences from spectra

As for our chromospheric inferences, Fig. 6 shows the retrieved line-of-sight magnetic field strengths using Eq. (3) on the

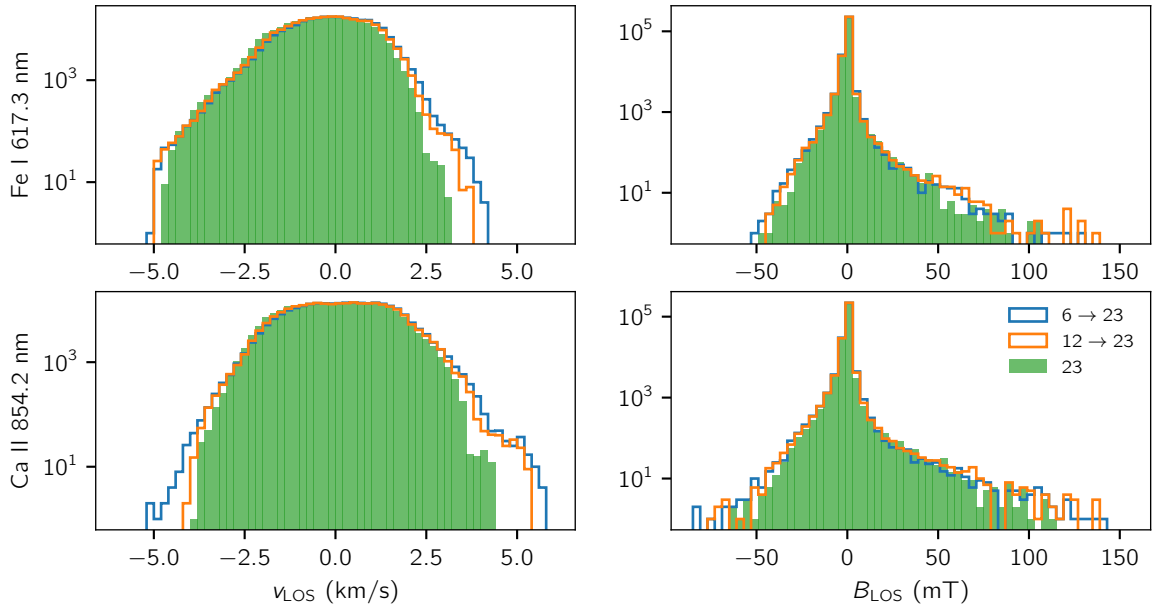

Fig. 5. Histograms of the inferred quantities using the COG method on the whole line profile for Fe I 617.33 nm (*top*) and Ca II 854.209 nm (*bottom*). We note that here, as in Fig. 7, we include the whole field of view for the simulation in the histograms, not only the quadrant shown in the colormaps elsewhere.

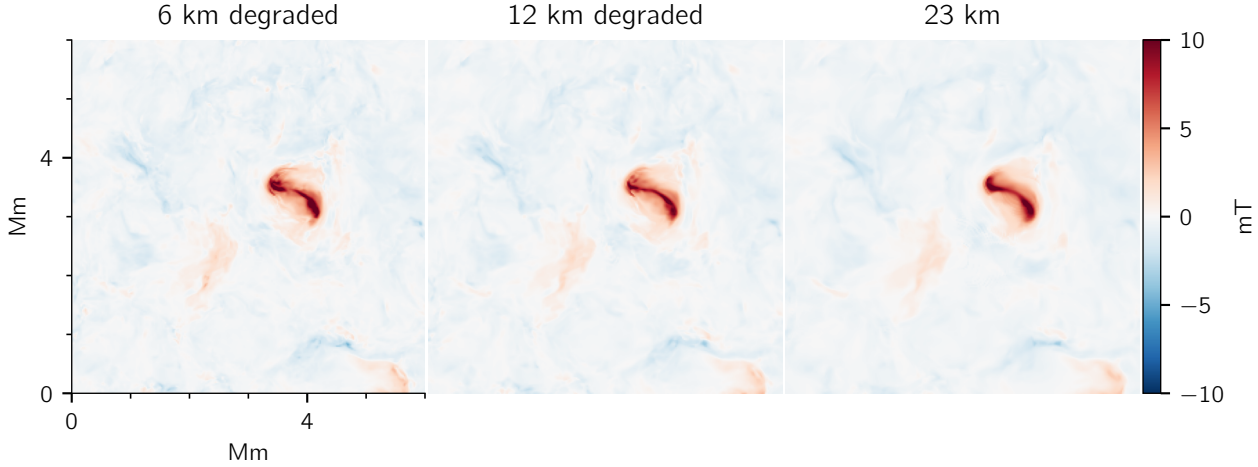

Fig. 6. Inferred line-of-sight magnetic fields for the core of the Ca II 854.209 nm line. The fields were estimated from Eq. (3) applied to the interval ±0.05 nm from the nominal center wavelength of the line. The layout is otherwise the same as in Fig. 3 and Fig. 4.

interval ±0.05 nm around the nominal line core. The differences between the resolution cases are not as dramatic here in the chromosphere as in the previously discussed photospheric estimates. Yet, looking closely at the main magnetic feature, we do see additional fine-structure and a concentration of the line-of-sight magnetic field with increasing resolution. The (logarithmic) distribution of the inferred line-of-sight magnetic field strengths obtained from this method is shown in Fig. 7; as with Fig. 5, this distribution also covers the whole horizontal range of the simulation, not just the highlighted quadrant in Fig. 6. The most salient aspect of this distribution is that, in contrast to the photospheric estimates of the line-of-sight magnetic field strength, the chromospheric inferences retain the tendency of getting more extreme from both 23 km to 12 km as well as from 12 km to 6 km in resolution. So while the most extreme values for the photospheric line-of-sight magnetic field seem to be reached already at 12 km resolution, the same is not the case for the chromospheric estimates which are still increasing in sync with the resolution.

3.4. Effects on inversions

We now turn our attention to the effects on quantities inferred from inversions. Our primary goal was not to perform the best possible inversions that most accurately reproduce the quantities from the simulations. Instead, we focus on the differential effects that arise from using spectra with varying amounts of subresolution effects. It may be possible to tweak and fine tune the parameters of the inversion to obtain a better overall fit, but we believe our inversion results are good enough for our purposes.

We show vertical cuts of inverted line-of-sight velocities, line-of-sight magnetic field strengths, and temperatures at two heights in Figs. 8–10, respectively. These were taken at $\log(\tau_{500}) = -3.9$ (top) and $\log(\tau_{500}) = -0.2$ (bottom). These

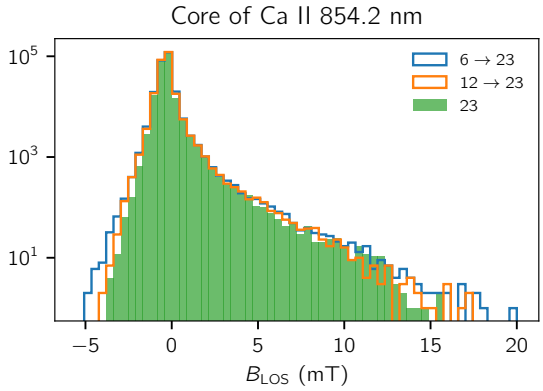

Fig. 7. Histograms of the inferred line-of-sight magnetic field strengths for the Ca II core after degradation to the common 23 km resolution, using the WFA method as given by Eq. (3). We note that here, as in Fig. 5, we include the whole horizontal extent of the simulation in the histograms, and not only the quadrant shown in the colormaps elsewhere.

heights are not directly comparable to either the previously shown simulation slices, or to the formation heights of the computed spectral lines. They were chosen to show the terrain in the low chromosphere and photosphere, respectively. In particular, the higher point is slightly below the mean $\tau = 1$ height of the Ca II line core. After this point, we are beginning to move outside the formation region of our two spectral lines, and therefore the inversions are not sensitive to these regions. For that reason, in our analysis we disregard regions with $\log(\tau_{500}) \lesssim -4$.

As before, we see more fine-structure with increasing resolution in all cases, here also for the temperature maps. From the 23 km to 12 km case, we also see the hotspots of increased extreme values in line-of-sight velocities and magnetic field strengths. Less pronounced, but still visible by inspection, is the same tendency comparing the 12 km inversion to the 6 km inversion. In particular, the photospheric line-of-sight velocities, and also the line-of-sight magnetic field strengths and (most faintly) the chromospheric line-of-sight velocities show these localized areas of increased extremes. For the temperatures, the tendency of increased extremes still holds going from 23 km to 12 km, but now we also note that some hotspots disappear from the maps along the way, that is some areas of extreme temperatures become smoother at higher resolution; for instance, this includes the bright (yellow) spots which are seen at $(x, y) \approx (2, 2)$ Mm in both 23 km panels, or $(x, y) \approx (3, 5)$ Mm in the lower panel of Fig. 10. Interestingly, from the 12 km case to the 6 km case, the variation in extreme areas does not appear to follow any particular trend, at least on visual inspection. This, together with the less pronounced variation in fine-structure, suggests a closer convergence in the retrieved temperatures than in the other atmospheric quantities.

The new element brought in by the inversions is the presence of obvious artifacts, both salt-and-pepper-like pixels that stand out as well as larger regions of more continuous over- and under-estimations. The latter type of artifacts are especially poignant around the regions of strong line-of-sight magnetic field strengths, where artificial regions of opposing polarity (not present in either the simulations or the simple inferences discussed earlier) are imposed around the real fields. These smooth regions are particularly intriguing when one considers that the STiC inversion code treats each column independently in a 1.5D fashion. These spurious regions are more frequent for 6 km than 12 km, suggesting that subresolution effects have a systematic impact that negatively affects the accuracy of inversions. This could be interpreted as the subresolution effects making it more difficult to reproduce the degraded spectra with a 1D plane-parallel atmosphere, since the individual atmospheric columns making up the pixel to be inverted span a broader range of conditions.

We show the distributions (number of pixels, color-coded on a logarithmic scale) of the inverted quantities versus their $\log(\tau_{500})$ in Fig. 11. The salient features of these images are the ranges and numbers of the uttermost extremes, and, most importantly, the steepness of the color gradient for the middling values. From this figure, it is apparent that more extreme line-of-sight velocities can be found for increasing resolution at all considered heights. Regarding the line-of-sight magnetic field strengths, one can see a wider distribution for the 6 km and 12 km case versus the 23 km case. Comparing the 6 km inversion with the 12 km inversion, the differences do not seem as large; however, importantly, there seems to be more negative line-of-sight magnetic fields present throughout the considered heights, which is in agreement with the increased amount of (artificial) negative field in Fig. 9. For the temperatures, the differences between 6 km and 12 km appear particularly small. From the distributions alone, it is not apparent that the 6 km inversion produces worse artifacts than the 12 km one, but comparing the photospheric inversion results with both the simulation variables and the inferences from the spectra shows that one of the effects of increasing the underlying spatial resolution is that inversions seem to converge on incorrect solutions, which introduce erroneous fields.

To quantify the reliability of the inversions with varying amounts of subresolution effects, we looked at the variation of the median absolute difference between the atmospheric quantities inferred from inversions and the corresponding simulation variables as a function of $\log(\tau_{500})$. We interpolated the line-of-sight magnetic fields, velocities, and the temperature for each of the three simulations to the $\log(\tau_{500})$ grid points of the inversions. We subsequently performed the same spatial degradation on these interpolated quantities as we did to the synthetic profiles. For each $\log(\tau_{500})$ iso-surface, we computed the median absolute difference between the inversion and the corresponding (degraded) simulation, normalized to the values for the 23 km runs. These median differences therefore give a statistical measure of how accurate inversions are at different depths, compared to a baseline set by the 23 km simulation, which has no subresolution effects. We show the results of this procedure in Fig. 12.

We find that subresolution negatively affects the reliability of inversions at nearly all optical depths, by about 10%. Compared to simulation variables degraded in the same way as the spectra used for inversions, the inverted variables are consistently worse when compared to the case with no subresolution, that is the 23 km run. There are some heights where the inverted and degraded atmospheres do match better in line-of-sight velocities and temperature for the higher-resolution cases. However, on the whole, the inclusion of subresolution imprints on the spectra to be inverted seems to reduce the accuracy of the inferred atmosphere by about 5–20%, and typically around 10%. All three quantities, that is the temperature, line-of-sight velocity, and line-of-sight magnetic field strength, are affected by similar amounts. The results for the 6 km simulation are worse than for the 12 km simulation, indicating that with increased subresolution, the inversions become less reliable. Encouragingly, the difference from 6 km to 12 km is much smaller than the difference from 12 km to 23 km, which suggests that we are converging on an upper limit. Although one should be careful since we only have two data points, it is worth noting that the results

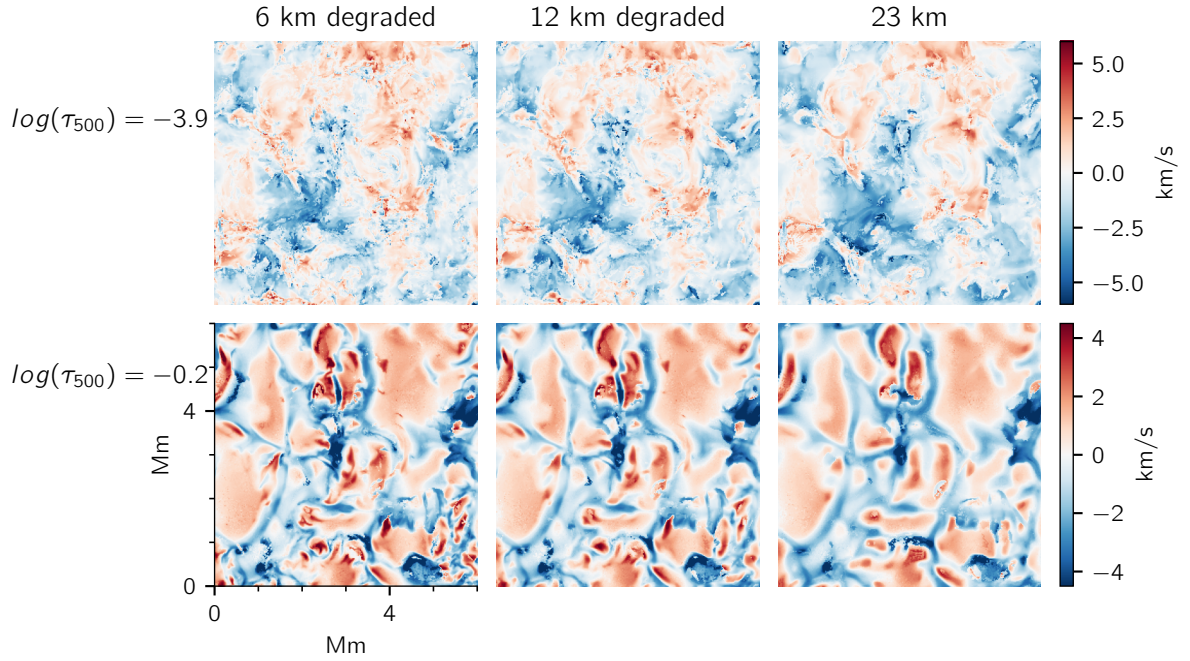

Fig. 8. Retrieved line-of-sight velocities from the inversions of the (degraded) spectra, taken at the heights $\log(\tau_{500}) = -3.9$ (*top*) and $\log(\tau_{500}) = -0.2$ (*bottom*), corresponding to the lower chromosphere and the photosphere, respectively.

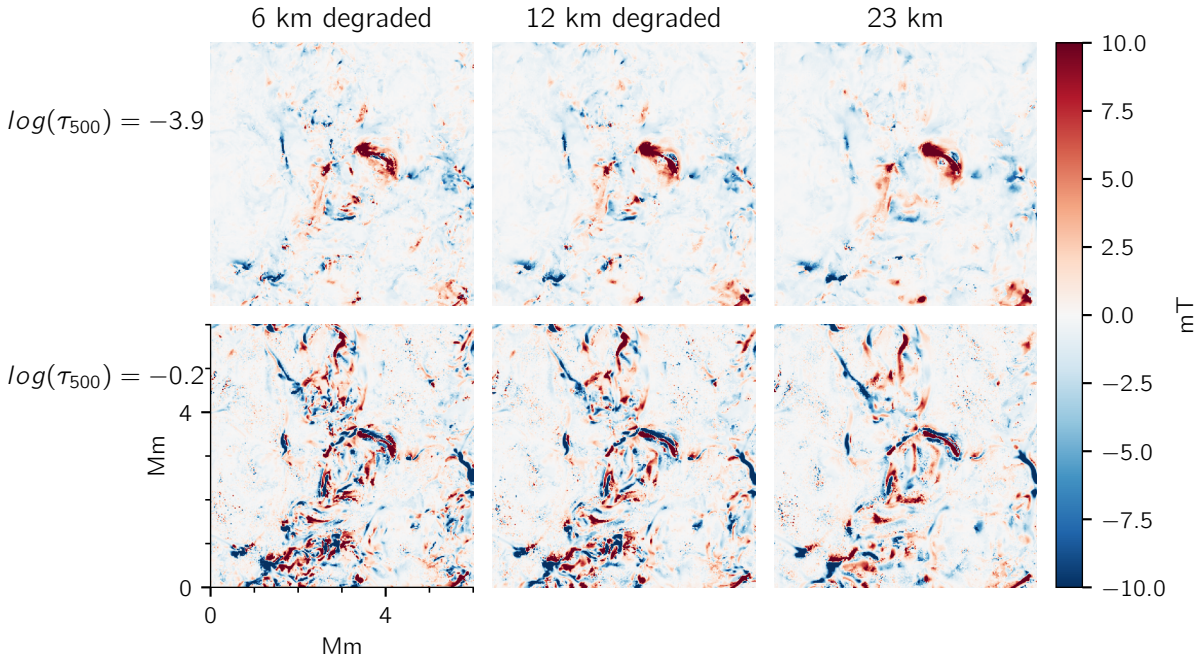

Fig. 9. Retrieved line-of-sight magnetic field strengths from the inversions of the (degraded) spectra, taken at the heights $\log(\tau_{500}) = -3.9$ (*top*) and $\log(\tau_{500}) = -0.2$ (*bottom*), corresponding to the lower chromosphere and the photosphere, respectively.

seem robust because the differences between 6 km and 12 km are consistent for different variables and across different depths, and that the median, taken over 512×512 points for each value of $\log(\tau_{500})$, neglects the more extreme "salt and pepper" cases where the inversions struggled. The fact that the results seem to vary a lot less from 6 km to 12 km is also consistent with the idea that adding more and more subresolution effects has a diminishing effect on the spectra since much higher resolution is strongly suppressed by the spatial convolution, and this results in subtler and subtler effects on the spectra.

4. Discussion and conclusions

Adopting a reference numerical grid size of 23 km pix^{-1}, we analyzed full Stokes spectra from three simulations with pixel sizes of 23, 12, and 6 km pix^{-1}, with the spectra from the latter two degraded to the reference resolution. The purpose was to build spectra with varying degrees of subresolution imprints. For the 23 km run, they are at the native resolution (no subresolution), for 12 km at half the native resolution, and for 6 km at a quarter of the native resolution. Our original question was to find how

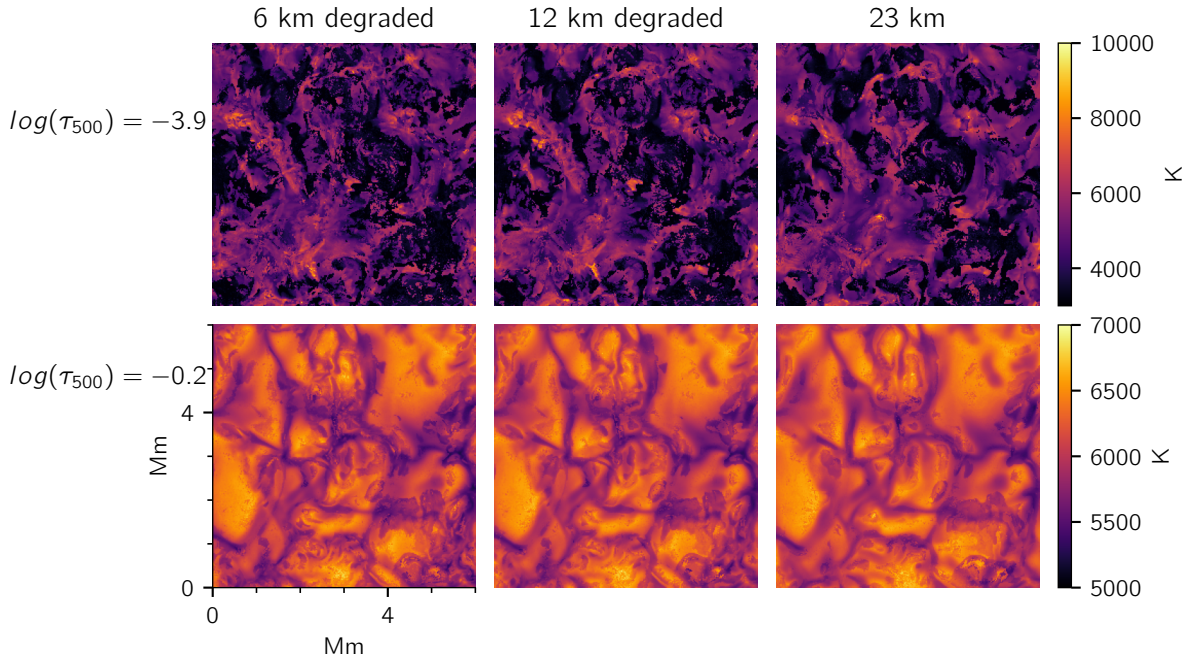

Fig. 10. Retrieved temperatures from the inversions of the (degraded) spectra, taken at the heights $\log(\tau_{500}) = -3.9$ (*top*) and $\log(\tau_{500}) = -0.2$ (*bottom*), corresponding to the lower chromosphere and the photosphere, respectively.

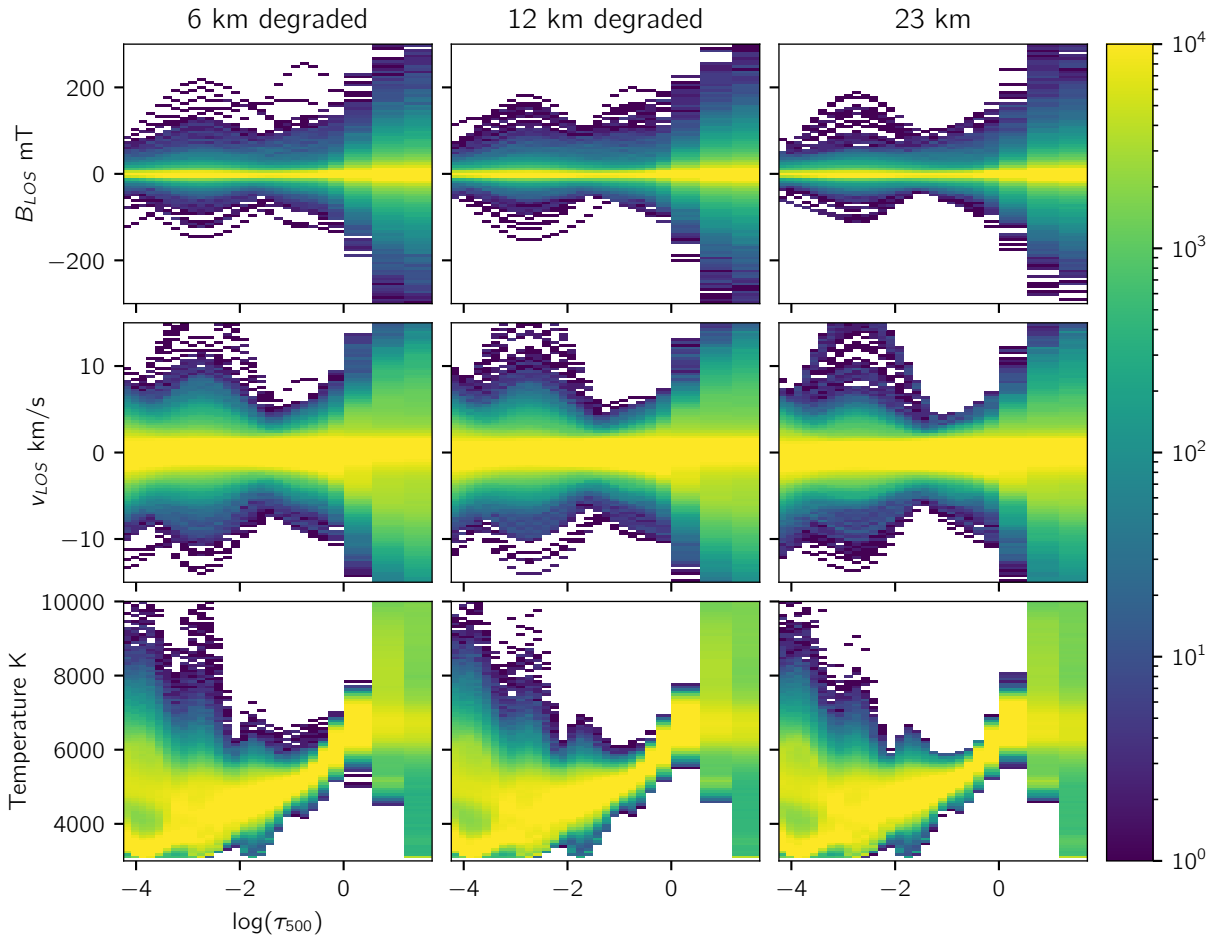

Fig. 11. Distribution (number of pixels) of retrieved line-of-sight velocities and magnetic field strengths, as well as temperature, for the inversions of the (degraded) spectra, taken at each considered $\log(\tau_{500})$ grid point of the inverted atmospheres. The color bar is logarithmic in the number of pixels, and saturated at 10^4.

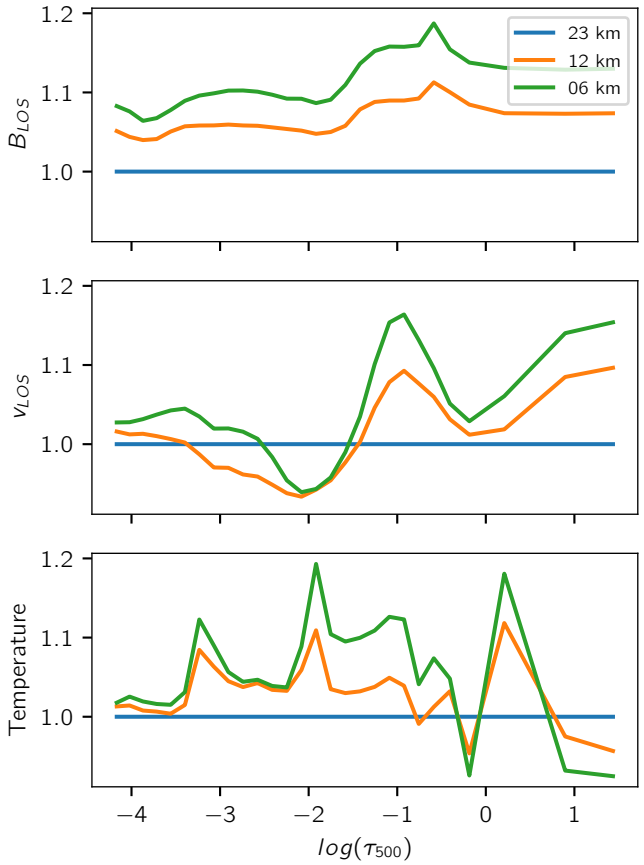

Fig. 12. Median absolute difference between inversion and simulation quantities taken at each considered $\log(\tau_{500})$ grid point of the inverted atmospheres. Normalized to the median absolute difference of the 23 km inversion and the 23 km simulation.

much these subresolution effects impact inferred quantities such as line-of-sight velocities and magnetic fields.

Our results show that simulations with different numerical resolutions do produce different results, and that these differences persist even after a spatial degradation of the emergent spectra. While the large-scale structures and tendencies remain the same between the simulations that have been considered here, the higher-resolution simulations produce fine-structure beyond that of the lower-resolution simulations, and this fine-structure still remains after applying a Gaussian convolution and downsampling. Furthermore, the atmospheric quantities inferred from the higher-resolution simulations show a higher occurrence of more extreme values when compared to the lower resolution simulations. From the distributions of the inferred quantities, we find that the trend of the extreme values increasing in tandem with the resolution clearly persists even up to the 6 km resolution in photospheric line-of-sight velocities and chromospheric line-of-sight magnetic field strengths. The same trend is less clear when it comes to the histograms of photospheric line-of-sight magnetic field strengths, however, as the 12 km and 6 km spectra give rise to comparable maximum values of the field. Still, even in this case, one can clearly see more fine-structure in the inferred photospheric line-of-sight magnetic field maps for the 6 km simulation when compared to the 12 km simulation.

When it comes to inversions, our results show a consistent and clear trend: subresolution leads to a systematic error. This error is not much, about 10%, but it is present at all heights and in the three variables analyzed here: line-of-sight velocity, line-of-sight magnetic field strength, and temperature. Our analysis is limited to resolutions that are typical of 1-m class telescopes, but with the power-law scaling of small structure in the solar surface (Abramenko et al. 2012), similar effects are likely to be present even with the next generation of 4-m telescopes.

It is important to be aware of the limitations of this work. Given how the simulations were devised and because we wanted to make a comparison on a pixel-by-pixel basis, we were limited in having only three resolutions, and we used only one snapshot for each resolution. Having a larger range of resolutions based on the same parent simulation would require additional relaxation, with the consequence that changes would develop in the evolution of the atmosphere and the fields of view would be different. In that case, only a statistical study would be possible. We also note that given how the simulations were built, the vertical resolution was not the same between the 23 km resolution and the other two, which had twice as many points. It is possible that some of the differences in the inversions arise from these changes in the vertical resolution and not solely because of the changes in horizontal resolution. Our spatial degradation was purely Gaussian, not following an Airy disk diffraction nor a point spread function (PSF) that could also include atmospheric seeing. Since the geometries of different instruments lead to different PSFs, we chose a Gaussian convolution since it is more neutral, and we believe the differences between an Airy pattern and the Gaussian function are negligible for our purposes, especially since the FWHM used are only 2 or 4 pixels. We also did not include any spectral degradation since our focus was on spatial resolution. Finally, we ran the inversions with a simple setup, which could have been better optimized. A more careful tweaking of the parameters could have led to better performance, but having the ground truth (the simulations) means that any adjustments using that knowledge are not neutral when compared to an inversion of real observations. This justified having a simple setup, also because our focus was on the differential effect of resolution in the inversions, and not on the absolute performance of the inversions, which are also subject to other sources of systematic errors.

To model phenomena extending to a given physical scale, one must choose a suitable numerical grid size. Numerical grid sizes are not directly comparable with observational resolution or pixel sizes. While a deep analysis of these differences is outside the scope of this work, we find that given the numerical diffusion present in these Bifrost experiments, a grid size of 23 km pix^{-1} is roughly equivalent to an observational resolution of about 100 km pix^{-1}. Notwithstanding the differences between numerical and observational pixel sizes, we argue that to mitigate for subresolution effects, it is best to aim for a numerical grid size that is about half that of the target value. If one assumes our equivalency of 100 km on the sun with a numerical grid of 23 km, our results indicate that a grid of 12 km would go a long way at mitigating small-scale structure that still leaks into inferred quantities. Aiming for a grid size four times smaller than the target value would give a more accurate result, but with diminishing returns, especially taking the much larger computational cost into account.

Acknowledgements. The authors would like to thank Jorrit Leenaarts, Rob Rutten and Oskar Steiner for giving helpful comments, questions and suggestions at preliminary talks about the contents of this manuscript, Åke Nordlund for useful comments regarding the effects of numerical diffusion, as well as Jaime de la Cruz Rodrígues for providing valuable help with setting up the STiC-inversions. We would also like to thank the anonymous referee for constructive and thorough feedback leading to several improvements of this manuscript. This work has been supported by the Research Council of Norway through its Centers of

Excellence scheme, project number 262622. Computational resources have been provided by UNINETT Sigma2 – the National Infrastructure for High Performance Computing and Data Storage in Norway.

References

Abramenko, V. I., Yurchyshyn, V. B., Goode, P. R., Kitiashvili, I. N., & Kosovichev, A. G. 2012, ApJ, 756, L27
Bello González, N., Franz, M., Martínez Pillet, V., et al. 2010, ApJ, 723, L134
Centeno, R. 2018, ApJ, 866, 89
Danilovic, S., Schüssler, M., & Solanki, S. K. 2010, A&A, 513, A1
de la Cruz Rodríguez, J., & van Noort, M. 2017, Space Sci. Rev., 210, 109
de la Cruz Rodríguez, J., Leenaarts, J., Danilovic, S., & Uitenbroek, H. 2019, A&A, 623, A74
de Wijn, A. G., Stenflo, J. O., Solanki, S. K., & Tsuneta, S. 2009, Space Sci. Rev., 144, 275
Gudiksen, B. V., Carlsson, M., Hansteen, V. H., et al. 2011, A&A, 531, A154
Holzreuter, R., & Solanki, S. K. 2013, A&A, 558, A20
Khomenko, E. V., Shelyag, S., Solanki, S. K., & Vögler, A. 2005, A&A, 442, 1059
Kritsuk, A. G., Nordlund, Å., Collins, D., et al. 2011, ApJ, 737, 13
Landi Degl'Innocenti, E., & Landolfi, M. 2004, Polarization in Spectral Lines, 307
Langangen, Ø., Carlsson, M., Rouppe van der Voort, L., & Stein, R. F. 2007, ApJ, 655, 615
Leenaarts, J., Carlsson, M., Hansteen, V., & Rouppe van der Voort, L. 2009, ApJ, 694, L128
Martínez González, M. J., & Bellot Rubio, L. R. 2009, ApJ, 700, 1391
Orozco Suárez, D., Bellot Rubio, L. R., Del Toro Iniesta, J. C., et al. 2007, PASJ, 59, S837
Pereira, T. M. D., & Uitenbroek, H. 2015, A&A, 574, A3
Pereira, T. M. D., Kiselman, D., & Asplund, M. 2009, A&A, 507, 417
Quintero Noda, C., Shimizu, T., de la Cruz Rodríguez, J., et al. 2016, MNRAS, 459, 3363
Quintero Noda, C., Shimizu, T., Katsukawa, Y., et al. 2017, MNRAS, 464, 4534
Schou, J., Scherrer, P. H., Bush, R. I., et al. 2012, Sol. Phys., 275, 229
Skumanich, A., & Lites, B. W. 1987, ApJ, 322, 473
Smitha, H. N., Holzreuter, R., van Noort, M., & Solanki, S. K. 2020, A&A, 633, A157
Smitha, H. N., Holzreuter, R., van Noort, M., & Solanki, S. K. 2021, A&A, 647, A46
Stein, R. F. 2012, Liv. Rev. Sol. Phys., 9, 4
Uitenbroek, H. 2001, ApJ, 557, 389
Uitenbroek, H. 2003, ApJ, 592, 1225
van Noort, M. 2012, A&A, 548, A5
Yadav, N., Cameron, R. H., & Solanki, S. K. 2020, ApJ, 894, L17